Acta Materialia 267 (2024) 119730

Contents lists available at ScienceDirect

Acta Materialia

journal homepage: www.elsevier.com/locate/actamat

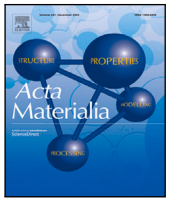

Full length article

Atomic cluster dynamics causes intermittent aging of metallic glasses

Zengquan Wang [a], Birte Riechers [a], Peter M. Derlet [b], Robert Maaß [a,c,*]

[a] Federal Institute of Materials Research and Testing (BAM), Unter den Eichen 87, Berlin 12205, Germany
[b] Condensed Matter Theory Group, Paul Scherrer Institut, CH-5232, Villigen PSI, Switzerland
[c] Department of Materials Science and Engineering, University of Illinois at Urbana-Champaign, Urbana, IL, 61801, USA

ARTICLE INFO

Keywords:
Metallic glasses
Aging
Molecular dynamics
XPCS

ABSTRACT

In the past two decades, numerous relaxation or physical aging experiments of metallic glasses have revealed signatures of intermittent atomic-scale processes. Revealed via intensity cross-correlations from coherent scattering using X-ray photon correlation spectroscopy (XPCS), the observed abrupt changes in the time-domain of atomic motion does not fit the picture of gradual slowing down of relaxation times and their origin continues to remain unclear. Using a binary Lennard-Jones model glass subjected to microsecond-long isotherms, we show here that temporally and spatially heterogeneous atomic-cluster activity at different length-scales drive the emergence of highly non-monotonous intensity cross-correlations. The simulated XPCS experiments reveal a variety of time-dependent intensity-cross correlations that, depending on both the structural evolution and the q-space sampling, give detailed insights into the possible structural origins of intermittent aging measured with XPCS.

1. Introduction

Glassy solids have a meta-stable structure that evolves with time. This gradual structural evolution towards an overall lower energy state involves thermally-activated structural rearrangements [1,2] and is typically referred to as physical aging [3]. Globally, aging may lead to minor changes in, for example density [4–6], hardness [7,8] or elastic moduli [4], whereas other macroscopic properties, such as toughness [5,9,10], can deteriorate significantly. The underlying structural processes that drive such property changes remain difficult to quantify, as they involve subtle rearrangements at the atomic scale. This can be resolved to some degree in conventional X-ray scattering experiments [7], but is well-documented in atomistic simulations of model glasses [11,12]. The latter gives detailed insights into possible local structural pathways that accompany the continued formation and growth of well-relaxed structural motifs, which often form an interconnected network of low-energy structures and pockets of energetically more frustrated regions [13–15].

A central problem in glass science is to formulate meaningful structure–property relationships that quantitatively connect the atomic-scale dynamics and transport with the macroscopic property-change during aging. In particular, amorphous systems with atomic-scale disorder, such as oxide glasses or metallic glasses (MGs), continue to challenge our structural understanding of physical aging, as it requires the time-dependent tracking of dynamics and transport of atoms that occur over a large range of structural time scales.

With the advent of coherent X-ray scattering, and in particular X-ray photon correlation spectroscopy (XPCS), this hurdle has now been (partly) overcome and glass dynamics can be probed as a function of time, temperature, and stress [16–19]. Relying on the time-dependent measurement of speckle patterns and their intensity cross-correlation as a function of waiting time, a variety of insights on the atomic-scale structural dynamics have been generated that were not accessible so far. For the here considered case of MGs, this includes the change of average relaxation times with time during isotherms [20–23], wave-vector dependent dynamics [24], or stress-driven atomic-scale dynamics [19,25,26].

One particular feature of structural dynamics derived from two-time correlation functions (TTCFs) of MGs or colloidal glasses, are strong fluctuations in the time-domain that are attributed to intermittent aging. First demonstrated for a Pd-based MG during cooling [27], intermittent aging or more broadly speaking strongly non-monotonously evolving momentary relaxation times, have now repeatedly been presented in the literature [19,25,26,28–30]. Remaining predominantly an experimental observation, our earlier work related to stress-driven structural dynamics in MGs proposed that a succession of heterogeneous microplastic activity in both space and time is the origin of the strongly non-monotonous correlation functions [19]. This remains as of today an interpretation, which motivates a more detailed assessment of possible microstructural processes that may underlie intermittent aging in MGs, or amorphous solids in general.

* Corresponding author at: Federal Institute of Materials Research and Testing (BAM), Unter den Eichen 87, Berlin 12205, Germany.
E-mail address: robert.maass@bam.de (R. Maaß).

https://doi.org/10.1016/j.actamat.2024.119730
Received 19 September 2023; Received in revised form 28 January 2024; Accepted 2 February 2024
Available online 6 February 2024

To address this shortcoming, we pursue here atomistic modeling of an aging binary model glass and simulate an XPCS experiment by the calculation of TTCFs during isothermal annealing around the glass-transition temperature, T_g. We find that (i) heterogeneous cluster dynamics of an evolving icosahedral and Frank-Kasper network during relaxation contributes to momentary fluctuations in the TTCFs, that (ii) significantly different TTCFs from one and the same structure arise when probing reciprocal space in 1, 2, or 3 dimensions (1D, 2D, or 3D), and that (iii) q-space selections across a fixed q-amplitude |q| but varying azimuthal positions give rise to significantly different evolutions of momentary time-scales. These results demonstrate the importance of q-range selections during XPCS and motivate large q-range sampling in one and the same experiment, because of the high sensitivity the method has for subtle atomic-scale dynamics. The main reason for intermittent aging seen in the TTCFs are atomic-scale clusters that rearrange during the continued network formation and evolution during energy relaxation. Thus, intermittent aging of MGs revealed with XPCS experiments is likely a combination of an extremely high resolved sampling of a specific structural length-scale and heterogeneous structural cluster rearrangements during relaxation in response to an external far-field stimulus.

2. Simulation methods and details

2.1. Molecular dynamics simulations

A model binary system described by a Lennard-Jones (LJ) potential and parameterized following Wahnström [31] is used to investigate the atomic-scale relaxation behavior along isothermal anneals of equivalent physical time scales of up to 2 μs. The interaction potential energy is given by

$$U_{ab}(r) = 4\epsilon\left[\left(\frac{\sigma_{ab}}{r}\right)^{12} - \left(\frac{\sigma_{ab}}{r}\right)^{6}\right], \tag{1}$$

where a and b are two different atoms, and r is their interatomic distance, $\sigma_{22} = 5/6\sigma_{11}$ and $\sigma_{12} = \sigma_{21} = 11/12\sigma_{11}$, where 1 and 2 denote different atom types. The atomic masses of the two atom types are arbitrarily chosen such that $m_1/m_2 = 2$. The distance unit is taken as $\sigma = \sigma_{11}$, the energy unit as ϵ, and the potential is truncated at the distance of 2.5σ. When more realistic metallic units, as for a prototypical glassy Zr-Cu alloy, are taken for ϵ and σ, one simulation time step corresponds to approximately 0.2 fs. In the present work we use this time-scale to present the time-dependent data. More details on the potential and its parametrization can be found in Refs. [32–34], with the difference that the here used simulation timesteps are smaller since simulations at higher temperatures were pursued.

Molecular dynamics (MD) simulations are executed with the LAMMPS software [35] using an NPT ensemble at fixed zero pressure. In this work, a 50:50 binary system consisting of atoms of type A and B, where A depicts the larger atom type, is heated to generate an equilibrium liquid state, and subsequently quenched to the different considered annealing temperatures with a cooling rate of 5×10^9 K/s. In what follows, the temperature T is expressed as the numerical value of the energy $k_B T$, where $k_B = 8.617 \times 10^{-5}$ eV/K, and therefore in the unit of ϵ instead of using the absolute temperature in the unit of Kelvin. Based on this, isothermal annealing is conducted at temperatures of 0.422, 0.414, 0.405, 0.396, and 0.388 for up to 10 billion MD timesteps (~2 μs). These temperature values are selected to represent states around the glass-transition regime, including the meta-stable undercooled liquid and the glassy solid regime of the binary LJ system. This aligns well with the typically probed temperature regime in XPCS experiments. Due to the strongly quenched-out structural dynamics and therefore unrealistically long simulation times, even lower temperature were not considered. An annealing at the temperature of 0.431 is also pursued to establish a reference of the stable equilibrium liquid state. We define time-zero for all annealing temperatures as the moment when the temperature reaches 0.431 during quenching. Visualizations of the atomic configuration and related structural analysis are pursued using OVITO [36] every 10 million MD time steps, corresponding to a time interval of about 2 ns. A modified Voronoi tessellation analysis is used to evaluate the local bonding topologies [33], which avoids the known overestimation of nearest neighbor atoms in the standard Voronoi approach. Analyzing the atomic connectivity and the identification of large atomic clusters based on bond connection criteria are done using the cluster analysis modifier in OVITO.

2.2. Simulating X-ray photon correlation spectroscopy

To investigate the structural and dynamical evolution of the isothermally annealed systems, TTCFs are calculated along each isotherm, mimicking the XPCS experiments. To this end, diffraction patterns are first calculated from the atomic configurations every 2 ns through

$$S(\boldsymbol{q}, t) = \frac{1}{N}\sum_{j,k}^{N} e^{-i\boldsymbol{q}\cdot[\boldsymbol{R}_j(t) - \boldsymbol{R}_k(t)]}, \tag{2}$$

where j, k are atoms and $\boldsymbol{q}$ is the wavevector in reciprocal space. Here we use a form factor equal to unity for all atom types to give equal weight to all atoms. The obtained diffraction patterns are subsequently used to conduct an intensity-intensity cross correlation via the calculation of a TTCF by

$$C(t_1, t_2) = \frac{\langle I(q, t_1) I(q, t_2)\rangle_q}{\langle I(q, t_1)\rangle_q \langle I(q, t_2)\rangle_q}, \tag{3}$$

where $\langle\cdot\rangle_q$ is the average over all chosen q-pixels in the diffraction pattern.

In standard XPCS experiments on MGs [19,24,25,27], a two-dimensional detector typically covers a narrow q-range, located around the first maximum of the diffraction pattern, therefore probing the lower medium-range order (MRO) length-scale of the glass. Specifically, the probed q-range in an experiment is of the order of 0.01–0.1 Å^{-1}, translating to a pixel resolution of ~10^{-5} Å^{-1}/pixel at a sampled scattering volume of the order of 10^3 μm^3. In the MD simulations pursued here, the scattering volume (represented by the simulation box) is ~$30 \times 30 \times 30$ σ^3 (approximately of the order of 10^3 nm^3 using metallic parameters for a Zr-Cu alloy), and the q-resolution is ~0.2 σ^{-1}/pixel, reflecting a smaller scattering volume and lower resolution than in experiments. However, simulations allow for a free choice of contributions from the diffraction sphere in reciprocal space, both in terms of angular position and in terms of its averaging. We exploit this advantage in the present work and sample the calculated diffraction data over 3, 2, and 1 dimensions across a q-range of 7–8 σ^{-1}(~2.3–2.7 Å^{-1} for Zr-Cu), covering approximately the full width at half maximum of the first main diffraction peak. More specifically, the 3D diffraction case covers a spherical shell within 7–8 σ^{-1} selected from the entire diffraction sphere, whereas the 2D-case covers a ring on the reciprocal plane where $q_x = 0$. The 1D-case covers a small (polygonal) area selected from the 2D pattern. In other words, both MRO and short-range order (SRO) components of the structure are tracked in the simulated XPCS experiments, because the first diffraction peak is used in the intensity cross-correlations.

3. Results and discussions

3.1. Structural evolution

The model glass was subjected to isothermal annealing over various durations at temperatures between 0.431 and 0.388, as summarized in the inset of Fig. 1. The annealing time exceeds 2 μs at $T = 0.422$ and $T = 0.388$, which is at least an order of magnitude longer than typical simulation times in MD simulations of model glasses. This long time scale allows tracking true thermally-activated structural relaxation [15,37] and has, despite the time-scale mismatch between

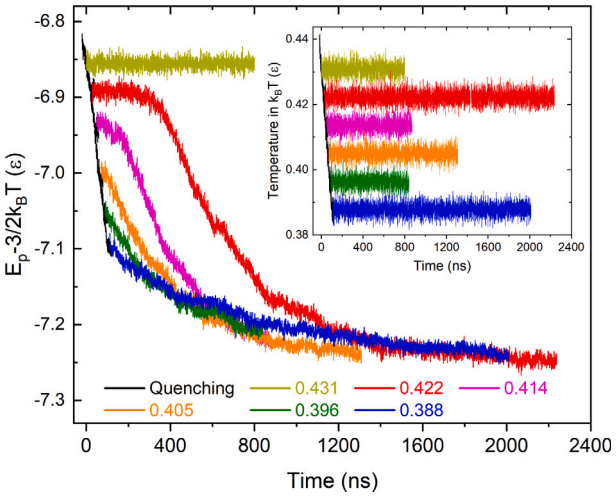

Fig. 1. The cohesive energy per atom vs. simulation time at different annealing temperatures. The inset depicts the quenching and different isothermal annealing protocols, where simulations at temperatures of 0.422 and 0.388 exceed approximately 2 μs physical time. (For interpretation of the references to color in this figure legend, the reader is referred to the web version of this article.)

experiments and computer simulations, a closer connection to experimentally observed structural dynamics than the often studied athermal processes seen in MD. To reduce computational costs, shorter annealing times of 0.8-1.3 μs were tracked at the temperatures of 0.414, 0.405, and 0.396, because of qualitatively similar observations (or mixtures thereof) made at $T = 0.422$ and $T = 0.388$.

Fig. 1 summarizes along all isotherms the cohesive energy per atom, $E_p - 3/2k_BT$, which corresponds to the average potential energy minus the average thermal potential energy component. At the annealing temperature of 0.422, the cohesive energy remains constant for about 250 ns, indicating a transition from the meta-stable super-cooled liquid towards a more relaxed state attained by continuous relaxation until the end of the anneal. While this transition occurs based on rearrangements of the disordered structure, the plateau includes a phase contribution in form of crystallization at the atomic scale, which is expected in simulations of this binary system in this temperature regime [38,39]. At lower annealing temperatures, the meta-stable liquid plateau, and therefore the contribution from latent crystallization, is absent and the cohesive energy reduction expectedly slows down. Irrespective of the annealing temperature, all cohesive-energy curves asymptote towards a final energy level. We will later see that this is due to an overall similar atomic fraction of low-energy structural motifs, albeit with strong differences in type of cluster, the degree of cluster connectivity, and their size.

Using the modified Voronoi tessellation and an associated bonding topology classification scheme [33], the structural evolution of the system is now considered. Here each local bonding topology is labeled as (N_4, N_5, N_6) where N_n is the number of n-fold bonds, i.e., bonds which contain n common neighbors. The coordination of such a structural motif is equal to $N_4 + N_5 + N_6$. Thus atoms with an icosahedral environment are labeled as (0, 12, 0), and those with a Frank-Kasper bonding environment are labeled as (0, 12, 4). Other Frank-Kasper environments are the (0, 12, 2) and (0, 12, 3) bonding topologies. As described elsewhere [33], icosahedral atoms are mostly of smaller size (atom type B) and atoms possessing Frank-Kasper environments are predominantly large atoms of type A in this model glass. Together, these structural motifs are labeled as Icosahedral-Frank-Kasper (IFK). The evolution of their fractions as a function of annealing time and temperature are summarized in Fig. 2, where the legend for all panels is displayed in Fig. 2c.

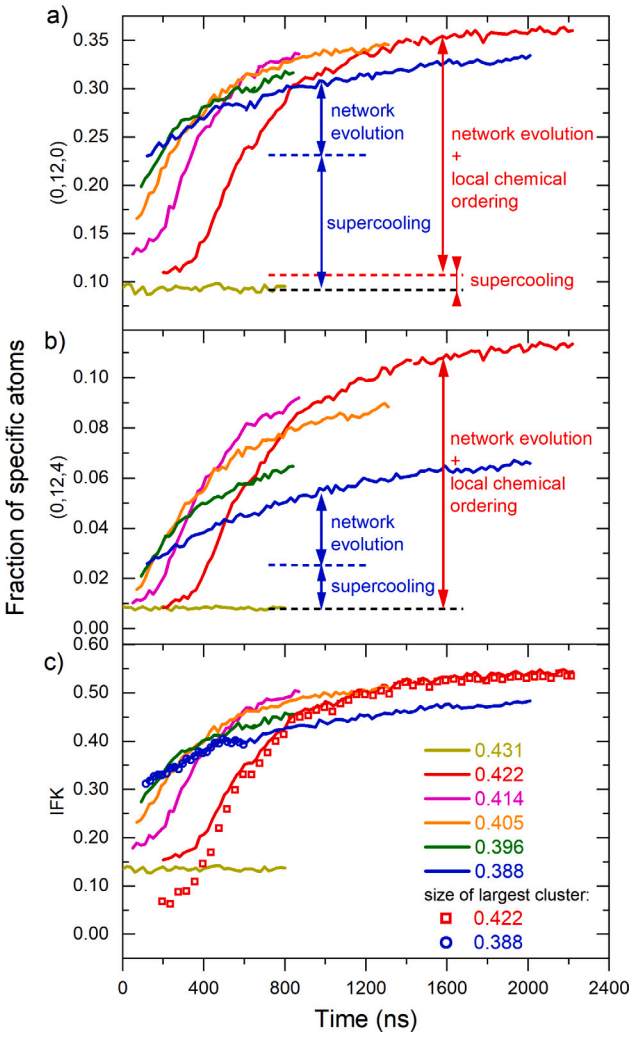

Fig. 2. Evolution of the fraction of specific atoms types vs. annealing time at different isothermal temperatures: (a) for icosahedral (0, 12, 0) atoms, (b) for Frank-Kasper (0, 12, 4) atoms, and (c) for all IFK atoms. Curves composed of symbols trace the development of the largest IFK cluster in size (in terms of overall atomic fraction) for temperatures of 0.422 and 0.388. Arrows between horizontal dashed lines and data traces indicate different evolutionary phases of the model glass during the annealing. The legend in (c) is applicable to all panels of this Figure. (For interpretation of the references to color in this figure legend, the reader is referred to the web version of this article.)

Fig. 2a shows the time-dependent evolution of icosahedral atom fraction across annealing temperatures. With increasing degree of supercooling, being smallest at $T = 0.422$ and largest at $T = 0.388$, different initial icosahedral fractions are presented, ranging between ~0.11 and ~0.23. In comparison with the equilibrium liquid state at $T = 0.431$, the fractional increase of icosahedral atoms due to supercooling grows from 2% at $T = 0.422$ to 14% at $T = 0.388$. Continued annealing leads to a temperature-dependent rate of icosahedral-fraction increase, which at longer annealing times exhibits small differences between temperatures of 0.422 and 0.388. However, the absolute difference in increase of icosahedral fraction is markedly different, amounting to 25% for $T = 0.422$ and 10% for $T = 0.388$ at 2000 ns, due to the different degree of network evolution and local chemical ordering at different temperatures.

Unlike the fraction of icosahedral atoms, whose initial value is sensitive to the degree of supercooling, the initial fraction of (0, 12, 4) Frank-Kasper atoms are all below 2.5%. Instead, its subsequent relative increase during annealing is 10.4% for $T = 0.422$ and 4.1% for

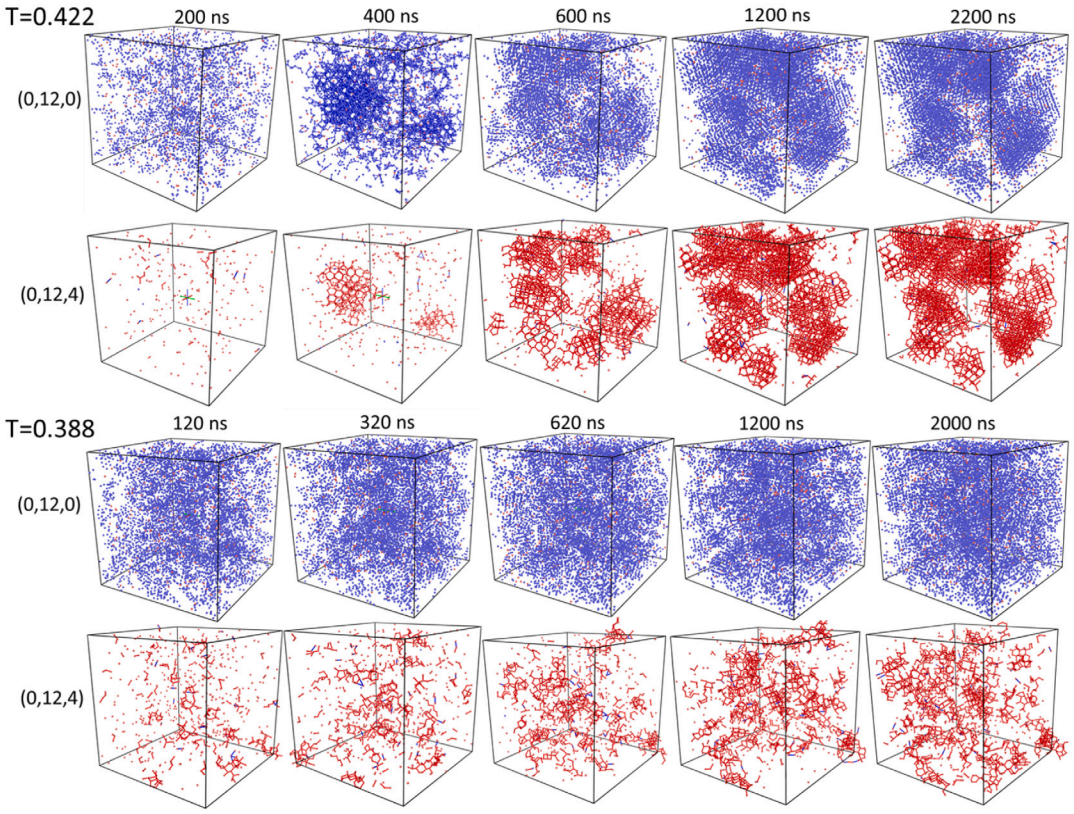

Fig. 3. Visualization of the icosahedral (0, 12, 0) and Frank-Kasper (0, 12, 4) atoms and their clusters/network at selected times for $T = 0.422$ and $T = 0.388$. A atoms are in red color and B atoms are blue. 6-fold bonds are colored in red and 5-fold bonds are in blue. (For interpretation of the references to color in this figure legend, the reader is referred to the web version of this article.)

$T = 0.388$ at 2000 ns with strongly different temperature-dependent rates in the first 800 ns, as shown in Fig. 2b, which is very similar to the icosahedral fraction increase. This shows how different structural components emerge and dominate depending on the annealing temperature.

The evolution of the total IFK fraction is shown in Fig. 2c. At all considered temperatures, an IFK fraction approaching 50% is reached during annealing, where the $T = 0.388$ anneal exhibits a distinctly higher initial fraction and lower rate of increase due to the large initial icosahedral fraction. In addition, the largest clusters at any time is identified using the OVITO Cluster Analysis modifier and its size in terms of atomic fraction is exemplarily displayed in Fig. 2c for $T = 0.422$ and $T = 0.388$ as a function of annealing time. Given that the size-evolution of the largest cluster at both these temperatures follows the total IFK fraction very closely, it becomes clear that the model glass relaxes via a continuously growing and connected IFK network.

The visualization of the evolving IFK network is shown in Fig. 3 for selected times at $T = 0.422$ and $T = 0.388$. Only the (0, 12, 0) and (0, 12, 4) atoms are visualized and neighboring atoms with the same label are connected to highlight the cluster evolution. It is clear that (0, 12, 0) atoms are mainly (>96%) B-atoms (colored in blue) and connected by 5-fold bonds shared by five neighboring tetrahedra, whereas (0, 12, 4) atoms are almost exclusively (>99%) A-atoms (in red) and connected by 6-fold bonds (in red) shared by six neighboring tetrahedra. These dominant clusters are displayed in Fig. 4, being B-atom centered distorted Z12 clusters (Fig. 4a) and A-atom centered Z16 clusters (Fig. 4b) [40].

Inspection of the structural snapshots during annealing summarized in Fig. 3 reveals initially isolated (0, 12, 4) fragments of 5 or less A-atoms up to 200 ns at the temperature of 0.422. At approximately 250 ns (not shown here), a larger cluster of 20 A-atoms has formed, that subsequently grows. This growth is driven by atom attachment or the

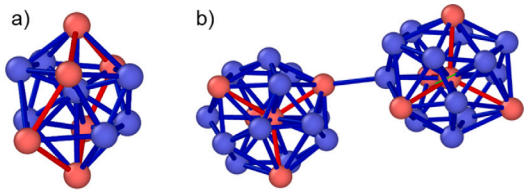

Fig. 4. Typical basic atomic cluster motifs identified in the relaxing systems: (a) one (0, 12, 0) B-centered and distorted icosahedral Z12 cluster; (b) Two connected (0, 12, 4) A-centered Z16 clusters. Bonds colored in red are 6-fold bonds and blue are 5-fold bonds. (For interpretation of the references to color in this figure legend, the reader is referred to the web version of this article.)

connection to other smaller clusters, the latter of which also involves the rotation of structural fragments. This is how an extended network of (0, 12, 4) Frank-Kasper A-atom-centered Z16 clusters develops during the annealing, while adjacent environments are filled with (0, 12, 0) icosahedral B-atom-centered distorted Z12 clusters (as shown in Fig. 4). These characteristic structural features, together with a stoichiometry of involved atoms close to AB_2, indicate the formation of C15 Laves phase fragments [40,41] and therefore atomic-scale formation of nanocrystallites. In fact, after 2200 ns annealing time at the temperature of 0.422, 22% of the A-atoms have become part of ordered Laves phase fragments.

Supercooling the melt to $T = 0.388$, gives rise to a much different structural evolution. Initially, the glass is also dominated by scattered (0, 12, 4) fragments. However, in comparison to the $T = 0.422$ structure at the beginning of the anneal, a larger number of (0, 12, 4) Frank-Kasper atoms and their Z16 clusters are present (Fig. 2b) after quenching to $T = 0.388$. These clusters coarsen much less than at $T =$

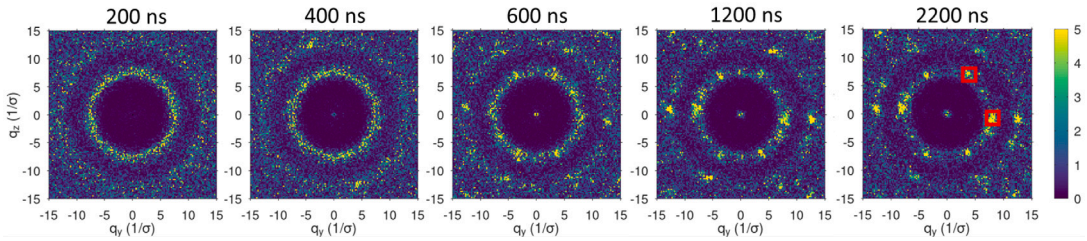

Fig. 5. Calculated 2D diffraction patterns for selected annealing times during the isothermal anneal at $T = 0.422$. Red squares in the diffraction pattern for 2200 ns indicate the approximate azimuthal locations where the q-pixels are selected for the calculation of 1D TTCFs for $T = 0.422$ in Fig. 6. (For interpretation of the references to color in this figure legend, the reader is referred to the web version of this article.)

0.422 and instead of the formation of Laves fragments, a percolation of small IFK motifs creates a system-spanning network. As we will see later, it is this difference in network evolution (dynamics) at different annealing temperatures that manifest itself in the corresponding XPCS simulations.

3.2. Wavevector-resolved structural dynamics

With this structural analysis as a function of annealing time at hand, the evolving model glasses are now investigated with respect to their structural dynamics as obtained with a simulated XPCS experiment. As a first step, 2D diffraction patterns are calculated, of which selected annealing times for $T = 0.422$ are exemplarily displayed in Fig. 5. Initially, diffuse scattering is observed and at 400 ns the first signs of emerging diffraction spots are seen. These Bragg spots evolve with annealing time both in terms of intensity, width, and position, reflecting the cluster coarsening and cluster rotation discussed above. The diffraction patterns at the lowest annealing temperature of 0.388 reveal diffuse diffraction rings throughout the entire anneal with a slight intensity redistribution at approximately 2000 ns (not shown here). The other annealing temperatures exhibit a mixture in diffraction intensity distribution as a function of time that falls in between these two extremes.

Based on the time series of diffraction data, TTCFs are calculated. Specifically, 3D, 2D, and 1D diffraction data is used, which represents differences in the q-space sampling and that leads to TTCFs as displayed in Fig. 6. The number of pixels chosen in q-space for the calculation are approximately 76000 for 3D diffraction patterns, 1055 for 2D patterns, and between 20 and 35 for 1D patterns. For the construction of the 1D TTCFs, two different and arbitrarily determined regions along the azimuth of 2D diffraction patterns were chosen to exemplify the sensitivity of the TTCF to the structural sub-sampling. Inspection of the TTCFs reveals a clear indication for increased data granularity with decreasing dimensionality and number of pixels of the q-space sampling. The 3D cases demonstrate annealing-time dependent broadening of the diagonal trace near the self-correlation, often connected to physical aging of the material. Based on the afore-discussed structural analysis, the underlying structural origin can now be assessed. At the highest two temperatures of 0.422 and 0.414, significant fractions of ordered Laves fragments and clusters form that contribute to long-lived Bragg intensities in the diffraction patterns, giving rise to persistently high contrast values at different waiting times. An example is the continued high contrast for all waiting times beyond approximately 1000 ns at $T = 0.422$, for which the structural analysis clearly revealed long-lived ordered atomic arrangements (Laves motifs and atomic-scale crystallization of the system). In contrast, at lower temperatures, broadening of high-contrast regions along the main diagonal of the TTCFs reflects physical aging, which structurally corresponds to the evolving IFK network without the formation of extended Laves motifs.

Using the 2D diffraction data for TTCF-calculations, a marked intermittency emerges. This is particularly prominent for the cases of $T = 0.414$ and $T = 0.405$, and the $T = 0.388$ anneal reveals a deceleration-acceleration phase of the dynamics during the second half of the annealing time. Linking the time-dependent structural analysis along the isotherms to the TTCFs gives evidence that strong contrast fluctuations as a function of annealing time (diagonal trace) or waiting time (horizontal trace) are caused by structural reorganization and subtle rotations of clusters during annealing. Such processes lead to diffraction intensity re-distributions that manifest themselves as the intermittent signatures in the TTCFs.

Reducing the q-space sampling to the 1D case, Fig. 6 demonstrates that intensity cross-correlations become very sensitive to the chosen q-range. The two presented 1D-cases cover the same radial range of 7–8 σ^{-1}, but are located at different azimuthal angles. For the arbitrarily chosen q-masks, very short-lived cross-correlations can be seen for the two cases at $T = 0.414$, whereas both $T = 0.405$ and $T = 0.422$ indicate longer structural correlations that persist beyond ~400 ns and ~1000 ns, respectively. This strong sensitivity of the TTCFs to the chosen q-range indicates how intermittent aging signatures and short-time fluctuations may arise due to subtle collective structural rearrangements and reorientation of cluster motifs at a given length-scale within the glass. This sensitivity of the TTCFs to the q-positions can be further highlighted by sampling along the azimuthal angle. Fig. 7, illustrates this for $T = 0.388$ and three different q-selections within 7–8 σ^{-1}. A shift of only 3 pixels yields significantly different dynamical signatures of the probed model glass. Such sub-sampling effects must be considered, when evaluating the so-called one-time correlation functions, $g_2(t)$, that averages the TTCF into a single time-dependent contrast decay.

From the above pursued simulations and the constructed TTCFs it is further possible to derive a time-averaged contrast decay as a function of waiting time. The resulting intensity autocorrelation functions, $g_2(t)$, being directly representative of the evolution of the corresponding intermediate scattering function, are displayed in Fig. 8. To this end, time windows encompassing the structural states for $T = 0.422$ and $T = 0.388$ highlighted in Fig. 3, and 3D q-space sampling according to the TTCFs of Fig. 6 were chosen. Strong contrast differences as a function of chosen time window emerge for $g_2(t)$ at $T = 0.422$ due to the development of stable structural motifs, such as the IFK network and Laves phase fragments. In particular the jump in contrast between the 600–800 ns and 1200–1400 ns time windows in Fig. 8a originates from the observed formation of ordered crystalline fragments during the high-temperature anneal. Given the large percentage of low-energy motifs, each selected time window, and with stronger degree the later stage isothermal evolution, only displays weak decorrelations. At the lower temperature $T = 0.388$, $g_2(t)$ of the glassy solid decorrelates at all times. Almost complete decorrelations are in fact seen for the early aging time windows, which indicates that relaxation times of the unrelaxed glass are well within the simulation time. Since the initial short-time plateau is at a time scale smaller than the chosen simulation time-resolution of 2 ns, it cannot be observed and corresponding fitting, as for example with the often used KWW function to extract equivalent relaxation times, is not meaningful. These insights given by $g_2(t)$ underline overall the significantly different dynamics in different temperature regimes. While the presence of the IFK-network and

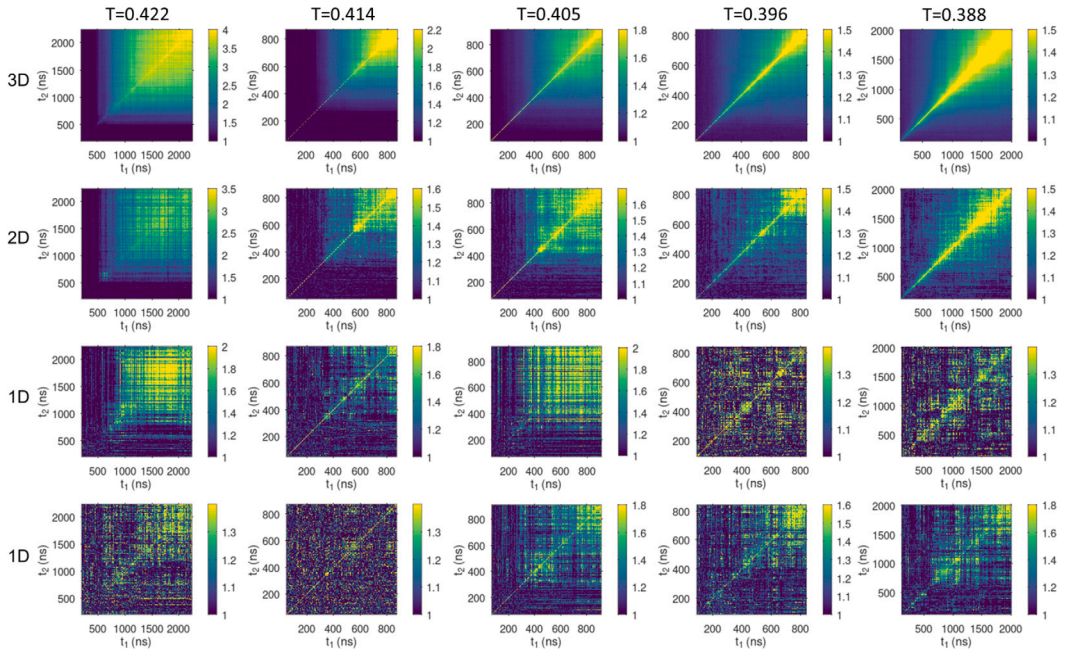

Fig. 6. TTCFs calculated from 3D, 2D, and 1D q-space sampling for all annealing simulations. Two 1D cases sampling the same q-range but different azimuthal positions along the diffraction ring are displayed (examples of azimuthal selection for 0.422 are marked with red squares in Fig. 5 at 2200 ns). Individual contrast ranges have been chosen for clarity. (For interpretation of the references to color in this figure legend, the reader is referred to the web version of this article.)

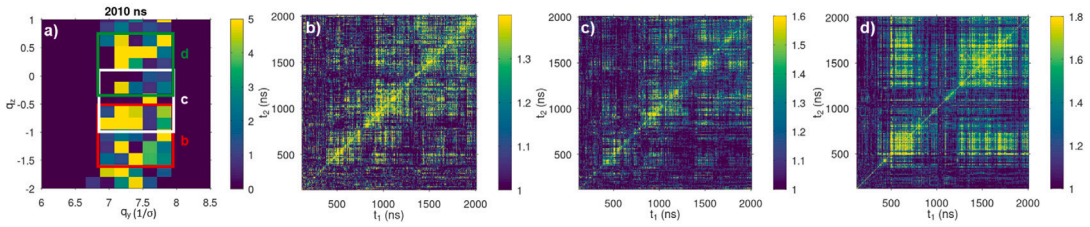

Fig. 7. (a) Selected part of the 2D diffraction pattern within 7–8 σ^{-1} at 2010 ns for the isothermal annealing at $T = 0.388$. (b), (c), and (d) 1D TTCFs calculated for the q-range selections denoted in (a). (For interpretation of the references to color in this figure legend, the reader is referred to the web version of this article.)

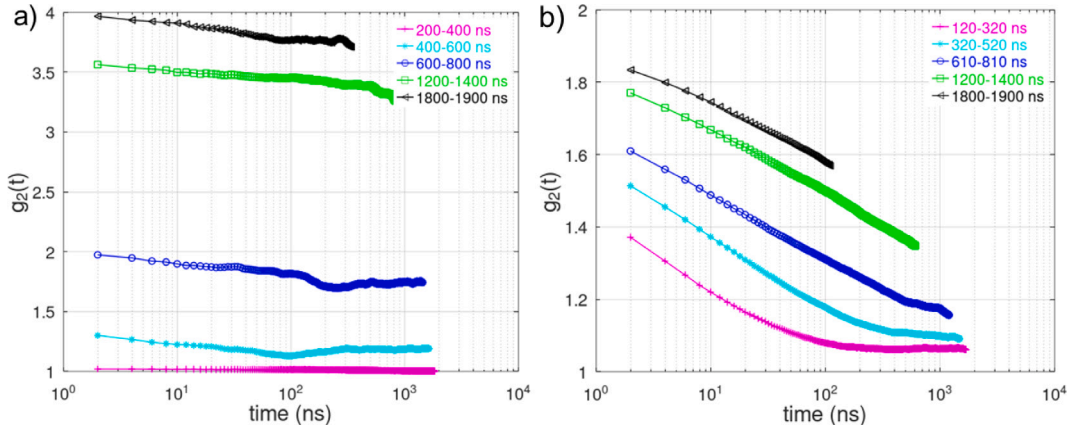

Fig. 8. $g_2(t)$ functions calculated from 3D TTCFs in Fig. 6 for (a) $T = 0.422$ and (b) $T = 0.388$. (For interpretation of the references to color in this figure legend, the reader is referred to the web version of this article.)

Laves-phase fragments at higher temperature eliminates much dynamic activity on the simulation time scale, the IFK-network development at $T = 0.388$ shows a gradual increase of the momentary relaxation time scale, reminiscent of the dynamics observed during homogeneous physical aging in experimental XPCS studies.

3.3. Separation of structural contributions

The role of the system spanning IFK network and Laves fragments in comparison to the non-IFK structural component becomes even more obvious when these contributions are separated, as can be done by the

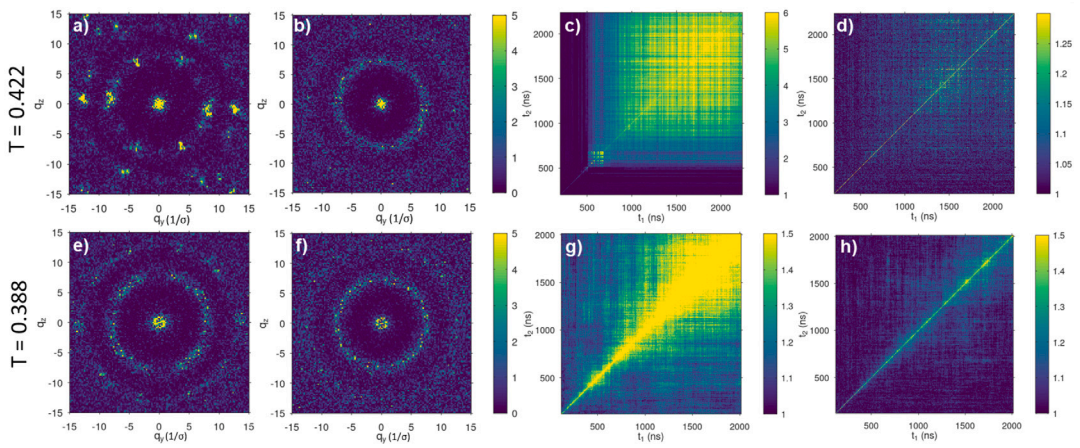

Fig. 9. 2D diffraction patterns obtained at 1200 ns from self-interference of (a) the IFK atoms and (b) non-IFK atoms and their respective contributions to the TTCFs [(c) and (d)] for the system isothermally annealed at $T = 0.422$. The bottom row shows the corresponding case at $T = 0.388$. (For interpretation of the references to color in this figure legend, the reader is referred to the web version of this article.)

calculation of their individual contribution to the diffraction patterns and TTCFs. Fig. 9 exemplifies this for $T = 0.422$ (Fig. 9a to Fig. 9d) and $T = 0.388$ (Fig. 9e to Fig. 9h). Structural snapshots at 1200 ns for the IFK network atoms (Fig. 9a) and non-IFK atoms (Fig. 9b) are calculated based only on their self-interference following Eq. (2), while the cross-interference between them is neglected. It is seen that higher diffraction intensities originate from the IFK network and very weak diffuse intensity distributions stem from the non-IFK domains. Consequently, their respective contributions to the full TTCFs (Fig. 9c and Fig. 9d) are slow intensity decorrelations in the case of the system-spanning IFK network, whereas the remaining structural component admits fast dynamics, which essentially is a stationary equilibrium liquid-like signature that within the time-scale sampling admits decorrelations over 1–3 pixels or 2–6 ns, depending on temperature. One can therefore conclude that most of the dynamical features seen in simulated TTCFs originate from cluster dynamics and extended network rearrangements rather than dilute transport mediated in the more frustrated arrangement of the model glass. In other words, microstructural dynamics of extended spatial domains must underlie intermittent aging dynamics and their long-time fluctuations are expected to give rise to the non-monotonous aging response seen experimentally with XPCS. We note that the lack of transport in the less frustrated domains is specific to the here tracked isothermal annealing times and that longer physical time-scales may give rise to sufficient and slow enough structural activity in the IFK domains, such that a stronger contribution to the TTCF can emerge.

The above outlined XPCS simulation and analysis of possible contributions from different structural components to the intensity cross-correlation can be further investigated by direct measurement of the typical time-scales associated with the icosahedral and Frank-Kasper structural environments. To this end and as a final step of our analysis, we follow 200 randomly chosen atoms with specific labeling at temperatures of 0.388 and 0.422. Icosahedral and Frank-Kasper atoms are identified at the end of the anneal and tracked backwards in time. This allows the construction of the data summarized in Fig. 10, where yellow indicates that the particular atom is either of icosahedral or of Frank-Kasper type. A dark blue color indicates the chosen atom is of different type than tracked. For both temperatures, continuous yellow lines for a given atom persist for the Frank-Kasper atoms, demonstrating their structural stability once formed in the relaxing glass. In contrast, significantly more interrupted yellow lines are seen for the icosahedral atoms, suggesting more temporally heterogeneous atomic-scale dynamics than that of the Frank-Kasper environments. This indicates that the long-lived contrast contributions seen in the TTCF predominantly arises from the Frank-Kasper part of the structure, further refining the analysis related to Fig. 9. Alternatively, it could be a result of the Voronoi tessellation being more sensitive to identifying the icosahedral environment, since one would expect icosahedral and Frank-Kasper stability to go hand-in-hand given the strong presence of C15 fragments and clusters.

To facilitate the interpretation of experimental XPCS data based on the here discussed simulation results, the cases of 1D and 3D q-space sampling are now considered. Before doing so, it is important to remember that a typical scattering volume in experiments is about nine orders of magnitude larger than in the above simulations. At the same time, experimental conditions are often limited to an available detector area covering a very narrow q-range. As a first limiting case of sampling the complete q-space, a TTCF is obtained that is based on a maximum of scattered intensities. This is not possible in experiments. However, the much larger experimental scattering volume compensates this difference by many more structural domains that fulfill the scattering condition compatible with the reduced q-range covered by the detector in experiments. Given the distinct contribution of the IFK-network to the TTCFs and their fluctuations, as demonstrated in Fig. 9, it is reasonable to conclude that a similar relative dominance of the structural components underlies the intermittent aging signature observed in experiments. The second limiting case is the 1D sampling in the simulations. In this case, TTCFs depend on the exact angular location of any specific $|q|$. This aspect is further underlined by Fig. 7, where smallest changes along the azimuthal direction yield clear differences in the resulting TTCFs, even though the entire diffraction peak is covered. Now, only a small number of atoms in the simulation cell contribute to the cross-correlation of the intensities, representing the highest degree of sub-sampling in terms of scattering intensities and q-range. A similar degree of sub-sampling is not expected in the experiments, because one probes at the maximum of the first peak of the structure factor, which in contrast to the simulations has a rather uniform intensity distribution at all azimuthal angles and contributions from many more scattering subvolume. In other words, the pronounced sub-ensemble effects in the TTCF as in Fig. 7 should not emerge. Instead, experiments yield intermittent intensity cross-correlation due to the narrower and more resolved q-range that reflect a high length-scale resolution. We are therefore concluding that the 3D simulations are best representing the experimental case in terms of TTCF-contrast, but not in terms of structural length-scale selectivity.

In this light, the simulations give a strong indication for that collective structural activity of clusters cause the reported intermittent dynamical signature in XPCS experiments. The exact type of collective structural dynamics underlying experimental short-time fluctuations in the TTCF remains unknown, but will range from localized γ-modes [42], via string-like excitations that are interpreted as the

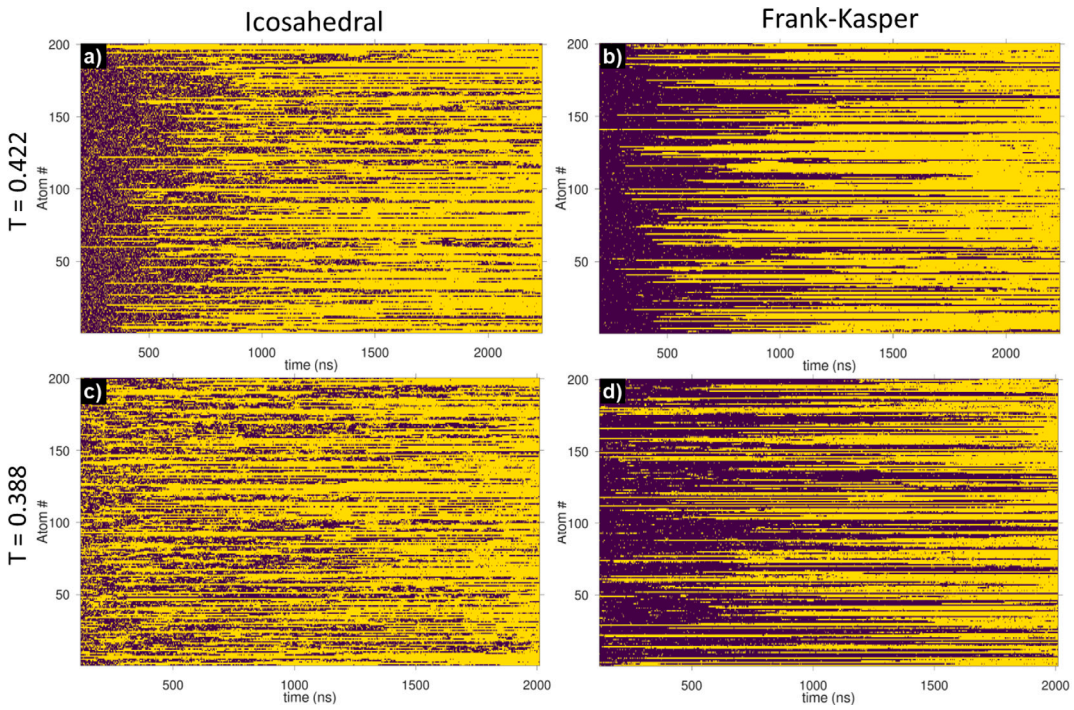

Fig. 10. The development of specific IFK atoms during annealing. 200 atoms were randomly chosen at the end of annealing at temperatures of 0.422 (top panels) and 0.388 (bottom panels). (a) icosahedral and (b) Frank-Kasper atoms at $T = 0.422$, and (c) icosahedral and (d) Frank-Kasper atoms at $T = 0.388$. Yellow indicates an atom is identified as icosahedral or Frank-Kasper type, whereas dark color indicates that the tracked atom does not belong to these structural groups at that given point in time. (For interpretation of the references to color in this figure legend, the reader is referred to the web version of this article.)

fundamental β-mode and known to mediate transport in this model glass [37], to extended cluster dynamics seen here, which also includes crystal-like fragments. Indeed, the latter are expected to be present in most cast MGs or may form during isothermal annealing experiments around T_g. As long as such structural features are not sufficiently averaged out in the correspondingly sampled X-ray speckles, abrupt changes in the intensity cross-correlations can emerge.

4. Summary and concluding remarks

In conclusion, the present work has investigated the origin of intermittent aging seen in X-ray photon correlation spectroscopy (XPCS) of (metallic) glasses using molecular dynamics simulations (MD). Specifically, XPCS experiments were simulated along various isothermal annealing traces at temperatures within the simulated glass transition temperature regime. Similar to XPCS experiments, calculated intensity cross-correlations along isotherms extending up to 2 μs physical time reveal strong intermittent signatures. A corresponding structural analysis demonstrates that the microscopic origin of abrupt contrast changes in two-time correlation functions (TTCFs) stems from in-time and in-space heterogeneous atomic cluster dynamics during energy relaxation of the studied binary model glass. Specifically, the continuous growth of the largest cluster by incorporating additional atoms and fragments of either icosahedral environments or Frank-Kasper motifs leads to atomic-scale dynamics that involves a larger number of atoms, which in turn leads to sufficient scattering intensity re-distributions as to cause abrupt changes in the corresponding TTCFs. At lower annealing temperatures, cluster dynamics is dominated by icosahedral and Frank-Kasper motifs, whereas at higher temperatures also fragments of chemically ordered Laves phases form. Extended clusters or networks of these dominating atomic configurations are contributing in the time-domain to persistent high contrast contributions in the TTCFs.

In addition to the micro-structural origin of intermittent aging, we reveal a marked q-dependence on the calculated TTCFs if two- or one-dimensional (2D or 1D) sampling of the diffraction space is done. In the case of sampling the full diffraction ring (2D case), intermittent aging is strongly driven by the small simulation volumes in the here conducted MD simulations. In fact, it would be worthwhile to experimentally construct TTCFs from larger q-ranges and different scattering volumes to identify up to which degree of spatial sampling intermittent dynamics persists. The simulated 1D case clearly shows how the choice of a given q-range may give strongly different results of the quantified atomic dynamics for different structural length-scales that are probed. This insight motivates future XPCS experiments of glassy solids in which a large q-range is sampled. Such wave-vector dependent tracking of structural dynamics would indeed fully leverage the method's advantage of quantifying sub-ensemble contributions to global aging. Furthermore, we conclude that measured at the local scale (narrow q-range), relaxation of metallic glasses will most likely always be intermittent to some degree, whereas sampling across sufficiently large inter-atomic length-scales regimes should eventually converge towards the macroscopically inferred gradual homogeneous aging response, as for example seen in stress-relaxation experiments [43–46].

Finally, the present work suggests that long-lived and extended network components – here summarized as the percolative icosahedral and Frank-Kasper (IFK) network – contribute most strongly to the TTCF-contrast. Non-IFK components of the studied model glass are mainly contributing to high contrasts in the self-correlation domain of a few ns of the MD-simulations. Whilst resolved at a different time-scale than experiments, this indicates the importance of correlated and collective atomic-scale dynamics in extended network components of experimentally studied glassy solids that is much beyond the simulation cell size in the present study. This emphasizes the role of a true glassy microstructure much beyond typically discussed MRO and SRO components.

CRediT authorship contribution statement

Zengquan Wang: Simulations, Formal analysis, Interpretation, Writing (original draft and editing), Visualization. **Birte Riechers:** Writing

(review and editing), Interpretation. **Peter M. Derlet:** Simulations, Software, Formal analysis, Interpretation, Writing (review and editing), Supervision. **Robert Maaß:** Writing (original draft, reviewing, and editing), Interpretation, Supervision, Resources, Funding acquisition.

Declaration of competing interest

The authors declare that they have no known competing financial interests or personal relationships that could have appeared to influence the work reported in this paper.

Acknowledgments

R.M. and B.R. gratefully acknowledge financial support by the European Union's Horizon Europe Framework Programme (HORIZON) under the Marie Skłodowska Curie grant agreement (No. 101063523). R.M. is grateful for financial support from the Federal Institute of Materials Research and Testing (BAM). P.M.D. acknowledges support by the Swiss National Science Foundation under the grant number 200021-165527.

References

[1] H.S. Chen, E. Coleman, Structure relaxation spectrum of metallic glasses, Appl. Phys. Lett. 28 (5) (1976) 245–247.
[2] L.C.E. Struik, Physical aging in plastics and other glassy materials, Polym. Eng. Sci. 17 (3) (1977) 165–173.
[3] Ian M. Hodge, Physical aging in polymer glasses, Science 267 (5206) (1995) 1945–1947.
[4] H.S. Chen, The influence of structural relaxation on the density and Young's modulus of metallic glasses, J. Appl. Phys. 49 (6) (1978) 3289–3291.
[5] Tsai-Wei Wu, F. Spaepen, The relation between enbrittlement and structural relaxation of an amorphous metal, Phil. Mag. B 61 (4) (1990) 739–750.
[6] Zach Evenson, Ralf Busch, Equilibrium viscosity, enthalpy recovery and free volume relaxation in a Zr44Ti11Ni10Cu10Be25 bulk metallic glass, Acta Mater. 59 (11) (2011) 4404–4415.
[7] W. Dmowski, C. Fan, M.L. Morrison, P.K. Liaw, T. Egami, Structural changes in bulk metallic glass after annealing below the glass-transition temperature, Mater. Sci. Eng. A 471 (1–2) (2007) 125–129.
[8] D. Pan, Y. Yokoyama, T. Fujita, Y.H. Liu, S. Kohara, A. Inoue, M.W. Chen, Correlation between structural relaxation and shear transformation zone volume of a bulk metallic glass, Appl. Phys. Lett. 95 (14) (2009) 141909.
[9] P. Murali, U. Ramamurty, Embrittlement of a bulk metallic glass due to sub-Tg annealing, Acta Mater. 53 (5) (2005) 1467–1478.
[10] Chris H. Rycroft, Eran Bouchbinder, Fracture toughness of metallic glasses: Annealing-induced embrittlement, Phys. Rev. Lett. 109 (19) (2012) 194301.
[11] Daniel B. Miracle, A structural model for metallic glasses, Nature Mater. 3 (10) (2004) 697–702.
[12] H.W. Sheng, W.K. Luo, F.M. Alamgir, J.M. Bai, E. Ma, Atomic packing and short-to-medium-range order in metallic glasses, Nature 439 (7075) (2006) 419–425.
[13] Tanaka Hajime, Roles of local icosahedral chemical ordering in glass and quasicrystal formation in metallic glass formers, J. Phys.: Condens. Matter 15 (31) (2003) L491.
[14] P. Ganesh, M. Widom, Ab initio simulations of geometrical frustration in supercooled liquid Fe and Fe-based metallic glass, Phys. Rev. B 77 (1) (2008) 014205.
[15] P.M. Derlet, R. Maass, Micro-plasticity in a fragile model binary glass, Acta Mater. 209 (2021) 116771.
[16] Mark Sutton, A review of X-ray intensity fluctuation spectroscopy, C. R. Phys. 9 (5) (2008) 657–667.
[17] Oleg G. Shpyrko, X-ray photon correlation spectroscopy, J. Synchrotron Radiat. 21 (5) (2014) 1057–1064.
[18] Qingteng Zhang, Eric M. Dufresne, Alec R. Sandy, Dynamics in hard condensed matter probed by X-ray photon correlation spectroscopy: Present and beyond, Curr. Opin. Solid State Mater. Sci. 22 (5) (2018) 202–212.
[19] Amlan Das, Peter M. Derlet, Chaoyang Liu, Eric M. Dufresne, Robert Maaß, Stress breaks universal aging behavior in a metallic glass, Nature Commun. 10 (1) (2019) 5006.
[20] B. Ruta, V.M. Giordano, L. Erra, C. Liu, E. Pineda, Structural and dynamical properties of Mg65Cu25Y10 metallic glasses studied by in situ high energy X-ray diffraction and time resolved X-ray photon correlation spectroscopy, J. Alloys Compd. 615 (2014) S45–S50.
[21] V.M. Giordano, B. Ruta, Unveiling the structural arrangements responsible for the atomic dynamics in metallic glasses during physical aging, Nature Commun. 7 (1) (2016) 10344.
[22] S. Kuechemann, C.Y. Liu, E.M. Dufresne, J. Shin, R. Maass, Shear banding leads to accelerated aging dynamics in a metallic glass, Phys. Rev. B 97 (1) (2018) 014204.
[23] Kaikin Wong, Rithin P. Krishnan, Eric M. Dufresne, Koji Ohara, Alec R. Sandy, Suresh M. Chathoth, Universal aging characteristics of macroscopically and microscopically dissimilar metallic glasses, Acta Mater. 155 (2018) 35–42.
[24] B. Ruta, S. Hechler, N. Neuber, D. Orsi, L. Cristofolini, O. Gross, B. Bochtler, M. Frey, A. Kuball, S. S Riegler, M. Stolpe, Z. Evenson, C. Gutt, F. Westermeier, R. Busch, I. Gallino, Wave-vector dependence of the dynamics in supercooled metallic liquids, Phys. Rev. Lett. 125 (5) (2020) 055701.
[25] A. Das, E.M. Dufresne, R. Maass, Structural dynamics and rejuvenation during cryogenic cycling in a Zr-based metallic glass, Acta Mater. 196 (2020) 723–732.
[26] Antoine Cornet, Gaston Garbarino, Federico Zontone, Yuriy Chushkin, Jeroen Jacobs, Eloi Pineda, Thierry Deschamps, Shubin Li, Alberto Ronca, Jie Shen, Guillaume Morard, Nico Neuber, Maximilian Frey, Ralf Busch, Isabella Gallino, Mohamed Mezouar, Gavin Vaughan, Beatrice Ruta, Denser glasses relax faster: Enhanced atomic mobility and anomalous particle displacement under in-situ high pressure compression of metallic glasses, Acta Mater. 255 (2023) 119065.
[27] Zach Evenson, Beatrice Ruta, Simon Hechler, Moritz Stolpe, Eloi Pineda, Isabella Gallino, Ralf Busch, X-Ray photon correlation spectroscopy reveals intermittent aging dynamics in a metallic glass, Phys. Rev. Lett. 115 (17) (2015) 175701.
[28] T.D. Xu, X.D. Wang, Q.P. Cao, D.X. Zhang, J.Z. Jiang, Aging behaviors in a La-based metallic glass revealed by two-time correlation functions, J. Phys. Chem. C 124 (41) (2020) 22753–22760.
[29] P. Luo, M.X. Li, H.Y. Jiang, R. Zhao, F. Zontone, Q.S. Zeng, H.Y. Bai, B. Ruta, W.H. Wang, Nonmonotonous atomic motions in metallic glasses, Phys. Rev. B 102 (5) (2020) 054108.
[30] Jake Song, Qingteng Zhang, Felipe de Quesada, Mehedi H. Rizvi, Joseph B. Tracy, Jan Ilavsky, Suresh Narayanan, Emanuela Del Gado, Robert L. Leheny, Niels Holten-Andersen, Gareth H. McKinley, Microscopic dynamics underlying the stress relaxation of arrested soft materials, Proc. Natl. Acad. Sci. 119 (30) (2022) e2201566119.
[31] Göran Wahnström, Molecular-dynamics study of a supercooled two-component Lennard–Jones system, Phys. Rev. A 44 (6) (1991) 3752–3764.
[32] Peter M. Derlet, Robert Maaß, Thermal processing and enthalpy storage of a binary amorphous solid: A molecular dynamics study, J. Mater. Res. 32 (14) (2017) 2668–2679.
[33] P.M. Derlet, Correlated disorder in a model binary glass through a local SU(2) bonding topology, Phys. Rev. Mater. 4 (12) (2020) 125601.
[34] P.M. Derlet, R. Maass, Emergent structural length scales in a model binary glass - The micro-second molecular dynamics time-scale regime, J. Alloys Compd. 821 (2020) 153209.
[35] Aidan P. Thompson, H. Metin Aktulga, Richard Berger, Dan S. Bolintineanu, W. Michael Brown, Paul S. Crozier, Pieter J. in 't Veld, Axel Kohlmeyer, Stan G. Moore, Trung Dac Nguyen, Ray Shan, Mark J. Stevens, Julien Tranchida, Christian Trott, Steven J. Plimpton, LAMMPS - a flexible simulation tool for particle-based materials modeling at the atomic, meso, and continuum scales, Comput. Phys. Comm. 271 (2022) 108171.
[36] Alexander Stukowski, Visualization and analysis of atomistic simulation data with OVITO–the Open Visualization Tool, Modelling Simul. Mater. Sci. Eng. 18 (1) (2010) 015012.
[37] P.M. Derlet, H. Bocquet, R. Maass, Viscosity and transport in a model fragile metallic glass, Phys. Rev. Mater. 5 (12) (2021) 125601.
[38] Ulf R. Pedersen, Nicholas P. Bailey, Jeppe C. Dyre, Thomas B. Schrøder, Crystallization of the Wahnström binary Lennard–Jones liquid, 2007, arXiv-cond-mat.mtrl-sci 0706.0813.
[39] Wenze Ouyang, Bin Sun, Zhiwei Sun, Shenghua Xu, Entire crystallization process of lennard-jones liquids: A large-scale molecular dynamics study, J. Chem. Phys. 152 (2020) 054903.
[40] Zhuocheng Xie, Dimitri Chauraud, Erik Bitzek, Sandra Korte-Kerzel, Julien Guénolé, Laves phase crystal analysis (LaCA): Atomistic identification of lattice defects in C14 and C15 topologically close-packed phases, J. Mater. Res. 36 (10) (2021) 2010–2024.
[41] F.C. Frank, J.S. Kasper, Complex alloy structures regarded as sphere packings. I. Definitions and basic principles, Acta Crystallogr. 11 (3) (1958) 184–190.
[42] S. Kuechemann, R. Maass, Gamma relaxation in bulk metallic glasses, Scr. Mater. 137 (2017) 5–8.
[43] Xiangfu Shi, Andrea Mandanici, Gregory B. McKenna, Shear stress relaxation and physical aging study on simple glass-forming materials, J. Chem. Phys. 123 (17) (2005) 174507.
[44] Laurence Ramos, Luca Cipelletti, Ultraslow dynamics and stress relaxation in the aging of a soft glassy system, Phys. Rev. Lett. 87 (24) (2001) 245503.
[45] Wei Hua Wang, Dynamic relaxations and relaxation-property relationships in metallic glasses, Prog. Mater. Sci. 106 (2019) 100561.
[46] Birte Riechers, Lisa A. Roed, Saeed Mehri, Trond S. Ingebrigtsen, Tina Hecksher, Jeppe C. Dyre, Kristine Niss, Predicting nonlinear physical aging of glasses from equilibrium relaxation via the material time, Sci. Adv. 8 (11) (2022) eabl9809.